Liquid Crystals
Publication details, including instructions for authors and subscription information:
http://www.informaworld.com/smpp/title~content=t713926090

Nuclear magnetic resonance of pretransitional ordering of liquid crystals in well defined nano-geometries: the utility of the Landau-de Gennes formalism

Xin Ma[a]; Gregory P. Crawford[b]; Renate J. Crawford[c]; Ichiro Amimori[d]; Slobodan Žumer[e]; Gregor Skačej[e]; Sylvain G. Cloutier[af]
[a] Department of Electrical Engineering, University of Delaware, Newark, DE, USA [b] College of Science & Department of Physics, University of Notre Dame, Notre Dame, IN, USA [c] Saint Mary's College, Notre Dame, IN, USA [d] Frontier Core Technology Lab., Fujifilm Corporation, Tokyo, Japan [e] Department of Physics, University of Ljubljana, Ljubljana, Slovenia [f] Delaware Biotechnology Institute, University of Delaware, Newark, DE, USA

First published on: 14 August 2009

To cite this Article Ma, Xin , Crawford, Gregory P. , Crawford, Renate J. , Amimori, Ichiro , Žumer, Slobodan , Skačej, Gregor and Cloutier, Sylvain G.(2009) 'Nuclear magnetic resonance of pretransitional ordering of liquid crystals in well defined nano-geometries: the utility of the Landau-de Gennes formalism', Liquid Crystals, 36: 10, 1229 — 1240, First published on: 14 August 2009 (iFirst)
To link to this Article: DOI: 10.1080/02678290903059263
URL: http://dx.doi.org/10.1080/02678290903059263

Liquid Crystals,
Vol. 36, Nos. 10–11, October–November 2009, 1229–1240

Taylor & Francis
Taylor & Francis Group

INVITED ARTICLE

Nuclear magnetic resonance of pretransitional ordering of liquid crystals in well defined nano-geometries: the utility of the Landau–de Gennes formalism

Xin Ma[a], Gregory P. Crawford[b]*, Renate J. Crawford[c], Ichiro Amimori[d], Slobodan Žumer[e], Gregor Skačej[e] and Sylvain G. Cloutier[a,f]

[a]*Department of Electrical Engineering, University of Delaware, Newark, DE 19716, USA;* [b]*College of Science & Department of Physics, University of Notre Dame, Notre Dame, IN 46556, USA;* [c]*Saint Mary's College, Notre Dame, IN 46556, USA;* [d]*Frontier Core Technology Lab., Fujifilm Corporation, Tokyo, Japan;* [e]*Department of Physics, University of Ljubljana, Jadranska 19, SI-1000 Ljubljana, Slovenia;* [f]*Delaware Biotechnology Institute, University of Delaware, Newark, DE 19716, USA*

(Received 24 April 2009; final form 26 June 2009)

The Landau–de Gennes (LdG) formalism has had a significant impact in many areas of physics and perhaps arguably most of all in understanding liquid crystals. In this review, we treat the utility of the LdG formalism in studying the ordering of liquid crystal systems confined at the nanoscale. The LdG formalism describes surface-induced ordering phenomena above the second-order phase transition point and predicts the disappearance of the nematic–isotropic transition into a continual evolution of order under certain conditions. We focus this paper on how the LdG theory has been used to understand ordering in well-defined nanoscaled environments, such as cylinders and ellipsoidal droplets, using deuterium nuclear magnetic resonance (^{2}H-NMR) to probe the evolution of order as it develops above the isotropic–nematic transitions and through the transition itself.

Keywords: liquid crystals; nano-confined geometries; paranematic phase; surface-induced ordering; polymer-dispersed liquid crystals; nanoporous alumina membrane

1. Introduction

A liquid crystal material in contact with a solid surface can be partially ordered even above the nematic–isotropic transition temperature where the bulk materials are isotropic. This phenomenon has been observed in many different liquid crystal systems over the years, such as in liquid crystal materials sandwiched between planar substrates or confined into restricted geometries. This observed ordering phenomenon above the isotropic–nematic transition temperature can be treated as orientational wetting of the substrate by the nematic phase at a temperature where the isotropic phase is stable in the bulk (*1–4*). On approaching the nematic–isotropic transition temperature (T_{NI}) from above, the thickness of the ordered nematic surface layer becomes a finite or infinite value corresponding to a partial or complete orientational wetting regime, according to the adsorption parameter Γ defined as:

$$\Gamma = \int_0^\infty S(z)dz, \qquad (1)$$

where z is the spatial distance from the order-inducing surface and $S(z)$ is the local orientational order parameter for the bulk liquid crystal (*5*). The surface-induced ordering in the isotropic phase is well described by $S(z)$ and the preferred molecular direction **n(r)** in the surface layer if biaxiality is ignored. If Γ diverges as T_{NI} is approached, the orientational wetting is known as complete. In contrast, the orienta tional wetting is said to be partial if Γ remains finite when approaching T_{NI}. The underlying nature of the wetting regime is strongly correlated to the interaction strength between the liquid crystal molecules and the orienting solid surface, and therefore depends on the magnitude of the surface-induced order parameter $S(z)$ in the interfacial layer (*5*, *6*). If the value of the surface order parameter S_0 exceeds a threshold order parameter S_c, then wetting is complete, while below S_c wetting is only partial. Within the Landau–de Gennes (LdG) framework, the threshold value is equal to the bulk nematic order parameter at T_{NI} (*2–4*).

The early work of Miyano demonstrated that the surface-induced order parameter could be accessed with optical experiments measuring the pre-transitional birefringence effects near the solid surface in planar systems (*7*, *8*). Follow-on experimental efforts included second-harmonic generation (*9*), field-induced twist (*10*), and evanescent-wave ellipsometry (*11*, *12*), which also demonstrated the existence of the

*Corresponding author. Email: Gregory_Crawford@ND.Edu

ISSN 0267-8292 print/ISSN 1366-5855 online

DOI: 10.1080/02678290903059263
http://www.informaworld.com

partially-ordered nematic layer above the T_{NI} at the solid surface.

In the early 1990s, it was found by Crawford *et al.* (*13*) that liquid crystals confined to Nuclepore cavities, well-defined channels penetrating through a polymeric membrane, could be infiltrated with liquid crystals and effectively probed with deuterium nuclear magnetic resonance (^{2}H-NMR). Since the surface-to-volume ratio in these confined systems was significant and the orientation of the liquid crystal in the Nuclepore cavities was uniform with respect to the static magnetic field, a small but measurable quadrupole splitting was observable well into the isotropic phase ($T - T_{NI} > 20$ K). This early investigation proved the usefulness of the ^{2}H-NMR technique in surface-induced order studies and showed that ^{2}H-NMR was capable of measuring S_0, the order parameter at the interface using the LdG formalism, the aligned interfacial layer thickness l_0, and the molecular exchange rate between the ordered surface layer and the bulk. Nuclepore systems were further used to confirm and monitor interesting configurations in the nematic phase (*14*), configuration transitions (*15*), and provided a measure of the saddle splay surface elastic constant (*16*, *17*).

The ^{2}H-NMR technique was later used to study liquid crystals confined into the channels of alumina-based Anopore membranes where anchoring transitions were observed and radically different values of S_0 were measured, depending on the surface alignment layer (*6*, *17–19*). The channels in the Anopore membranes are 200 nm in diameter, approaching the nanoscale. This work has recently been extended to smectic liquid crystals where nuclear magnetic resonance (NMR) can measure the degree of smectic–nematic coupling (*20*) and pretransitional smectic layering phenomena (*21*). The pretransitional smectic layering was observed in discrete and discontinuous steps as the smectic A–isotropic transition was approached from above. The LdG formalism was used to model this behaviour in much the same way as the nematic–isotropic phase transition (*21*).

In fact, the NMR technique has been applied to numerous other confined liquid crystal systems, including Vycor glass (*22–24*), silica aerogel (*25*), and Millipore filters (*26*). NMR has been used to probe the ordering of mesogenic molecules deposited on the cavity walls of an Anopore membrane surface (*27*). In addition to the intensive efforts devoted to liquid crystals confined to cylindrical and random geometries (*18*), the surface parameters of polymer dispersed liquid crystals (PDLCs) have also been investigated (*28*). Golemme *et al.* (*29*, *30*) also used ^{2}H-NMR to study spherical liquid crystal droplets. In their pioneering publications on NMR to study PDLCs, a weak first order nematic–isotropic transition was replaced by a continuous evolution of order for small droplets on the nanometre scale. This phenomenon was predicted many years before by Sheng in planar samples (*31*), and later by Vilfan *et al.* (*32*) in spherical droplets. Studies of PDLC droplets have continued on for more than a decade after the seminal publication of Golemme *et al.* (*29*, *30*). For example, NMR relaxometry was used to extract the value of S_0 from the transverse relaxation rate $T_{2\text{-}1}$ (*32*). Typically, the ability to precisely measure S_0 directly from the ^{2}H-NMR quadrupole splitting frequency in PDLC systems remains challenging for two reasons: (1) the director average orientation of the symmetry axis of a liquid crystal differs from one droplet to another with respect to the magnetic field direction; and (2) there tends to be a much larger droplet size distribution in PDLCs compared to the well-defined pores of Nuclepore and Anopore membranes (*6*, *15–19*, *33*).

With the expansion in computing power, as well as the increased sophistication of simulation techniques, strongly-confined liquid crystal systems are becoming increasingly accessible to computer simulation studies. In particular, a lot of effort has been invested in exploring nematic ordering inside PDLC droplets (*34*), where most of the analyses were based on the computationally-simple Lebwoh–Lasher lattice model. Typically, Monte Carlo simulations were carried out for this model system (*35*). The computational output can be expressed in terms of suitable order parameters or directly in terms of macroscopic experimental observables, such as ^{2}H-NMR spectra. The methodology for calculating dynamic NMR spectra, which is capable of handling fluctuations of molecular long axes and translational diffusion, has been presented and tested for spherical PDLC droplets (*36*). More recent Monte Carlo investigations of nematic ordering also extend to elliptical droplets (*37–40*). Most recently, computational methods have been extended to the ordering of hard rods confined to the surface of elongated nano-particles using grand canonical computer simulations (*41*).

There have been a number of other systems emerging in the literature most recently. For example, suspended clay particles have been shown to increase the isotropic–nematic transition temperature (*42*), where the particles' self-assemblies are ascribed to promote ordering above the bulk nematic–isotropic transition temperature. The infiltration of nematic liquid crystals into the voids of periodic structures, such as synthetic opals, where the interstitial regions between the spheres create nano-confined geometries for liquid crystals, has also been studied (*43*). In another extreme case, discotic liquid crystal materials have been confined to multi-walled carbon nanotubes and captured with polymerisation, where transmission electron

microscopy (TEM) revealed the captured order in the liquid crystal (*44*).

In this contribution we review two systems, both well-defined geometries on the nanoscale, which have been probed by ^{2}H-NMR. The two systems are nano-confining cylinders and ellipsoidal droplets. Because of their well-defined confinement at the nanoscale, these systems bring unique features to the study of pretransitional ordering in liquid crystal systems due to their uniform geometry and therefore accessibility to the NMR technique. In addition, both systems can be well described using the LdG formalism. We first review confinement effects in a cylindrical nanopore template system, much like the Anopore system described above, but created using an electro-chemical process (*45*). In this case, the channels were nearly a factor of ten smaller than earlier studies on Anopore membranes and highly-uniform in size distribution, providing an ideal platform to study confinement effects using NMR (*45*). Secondly, we will discuss confinement effects in an elliptical PDLC system that gives a reasonable quadrupole splitting in the isotropic phase. After PDLC formation using the emulsification technique (*46*), the PDLC film is subjected to a high degree of uniaxial strain (as much as 400%) to create ellipsoidal droplets whose droplet director and cross section are nearly uniform (*47*). These well-aligned droplet samples developed for light-scattering polariser applications create an ideal system to be studied with ^{2}H-NMR (*47*). We present an experimental determination of the surface-induced order parameter S_0, directly obtained from the quadrupole splitting frequency measured above T_{NI}. The experimental work is complemented with quadrupole splitting data from Monte Carlo simulations (*39*, *40*). This system is unique from the standpoint that the polymer wall of the PDLC cavity induces higher degrees of ordering when moderate strains are induced during the fabrication process.

On the theoretical front, these systems are novel from the standpoint of the earlier work of Sheng, who predicted both changes in the nematic–isotropic transition and an intermediate ordering transition behaviour (*3*) based on the competition between substrate potential (represented by the dimensionless substrate potential g as defined in (*3*)) and elastic forces from the volume represented by the critical thickness parameter R/ξ_0 defined in (*3*) (where R is the thickness of the liquid crystal film, here the radius of the cylindrical pores or PDLC spheres, and ξ_0 is a material-dependent correlation length parameter for second-order phase transition systems). All the phase transition regimes predicted by Sheng using the LdG theory are summarised in Table 1 (*3*). While a residual surface-induced paranematic ordering can be observed, it was predicted that bulk-like (discontinuous) phase transition behaviours will still observed if either (a) the substrate potential is too small or (b) the volume is too large. According to the same theory, the bulk-like phase transition behaviour should completely disappear and the transition should become continuous if (c) the substrate potential is too large compared to the elastic forces from the volume. Interestingly, this model also predicts a regime where (d) the right balance between substrate potential and elastic forces leads to a bulk-like phase transition in the volume while being completely suppressed at the interface.

2. ^{2}H-NMR spectroscopy of nano-confined αd$_2$-5CB liquid crystal

Deuterium nuclei are often used as a probe in studies of molecular structure and dynamic liquid crystal systems. This has proven useful in basic studies of ordering and phase transitions and to the understanding of confined liquid crystals treated in this contribution. For investigation of those nano-confined systems, we chose the well-understood 5CB (4′-pentyl-4-cyanobiphenyl) liquid crystal deuterated in the α-position on the hydrocarbon chain (αd$_2$-5CB) (*6*, *19*, *48–51*). Indeed, the ^{2}H-NMR spectroscopy on a bulk αd$_2$-5CB liquid crystal generates a quadrupolar frequency splitting $\delta\nu$ directly proportional to the degree of orientational order of the deuterated C–D bond with respect to the static magnetic field described by

$$\delta\nu(\mathrm{r}) = \frac{\delta\nu_B}{S_B} S(\mathrm{r}) \left[\frac{3}{2}\cos^2\theta_B(\mathrm{r}) - \frac{1}{2}\right], \qquad (2)$$

where $\theta_B(\mathbf{r})$ is the angle between the local nematic director and the magnetic field, $S(\mathbf{r})$ is the local order

Table 1. Phase transition regimes predicted by Sheng using the LdG theory applied to surface-aligned liquid crystal systems (*3*). For a detailed definition of quantities in the left column see (*3*) and the text.

	(a)	(b)	(c)	(d)
Dimensionless substrate potential g	<0.012	>0.012	>0.012	>0.012
Critical thickness parameter R/ξ_0	Independent	>65	<26	26–65
Averaged order parameter $<S>$	Discontinuous	Discontinuous	Continuous	Discontinuous
Surface order parameter S_0	Discontinuous	Discontinuous	Continuous	Continuous

parameter, $\delta\nu_B/S_B$ is the ratio between the quadrupole splitting frequency and the order parameter of the bulk nematic phase is ~87.5 kHz (*10*). For 5CB, the magnetic coherence length $\xi_m B^{-}(\mu_0 K\Delta\xi)^{1/2}\sim 1.1$ μm for reported values of $\Delta\xi = 1.2\times10^{-7}$, the anisotropy of the diamagnetic susceptibility $K = 6\times10^{-12}$ N, the elastic constant, $\mu_0 4\pi\times10^{-7}$ N A^{-2} and B is the scalar magnetic field. Typically, the permeability of free space ξ_m is significantly larger than our droplet/cylinder radii R, so that the field has no appreciable aligning effect. Furthermore, the characteristic length of diffusion in a NMR measurement is $d \approx (D/\delta\nu)^{1/2}$. Here $D \sim 10^{-11}$ m^{-2} s is the diffusion constant and $\delta\nu$ is a characteristic frequency in the NMR spectrum. In the nematic phase one has $\delta\nu \approx \delta\nu_B = 52.1$ kHz yielding $d \approx 44$ nm, while in the isotropic phase one obtains $\delta\nu \approx 500$ Hz and $d \approx 450$ nm. In our case, $d >> R$ in the isotropic phase for both the droplet and cylinder systems, so that we can expect complete diffusional averaging. The orientational order parameter measured with NMR is subsequently modelled using the LdG formalism (*52*). Equation (2) assumes an asymmetry parameter equal to zero, which is typical for bulk uniaxial liquid crystals, but not necessarily the case for strongly-confined systems (*53*). While this biaxiality effect is generally small and can be safely neglected in most cases (*54*), a non-zero asymmetry (or biaxiality) would generate clear signatures in the ^{2}H-NMR spectra (*53*, *55*).

The following sections illustrate how ^{2}H-NMR spectroscopy can be applied to investigate the molecular organisation and phase transition behaviour of the well-documented deuterated-5CB liquid crystal in two strongly-confined geometries. In the first case, an anodic aluminium oxide (AAO) membrane with highly-uniform periodically-distributed cylindrical pores was used as the confining template. In the second case, the same liquid crystalline material was confined into nanoscale-sized PDLC droplets geometries.

3. Surface-induced ordering in cylindrical nanocavities

Several experimental studies used cylindrical cavities as confining structures, since they make the analysis of the system significantly simpler (*6*, *12–18*, *45*, *48*, *56–60*). Two commercial nanopore membranes commonly used for cylindrical confinement are the Nuclepore and the Anopore membranes (*56*, *57*). However, the Nuclepore non-uniform pore diameters range from 15 nm up to 12 μm and such a broad pore-size distribution produces a strong spectroscopic signal averaging. On the other hand, the Anopore has uniform 200 nm-diameter pores (*48*), which limits

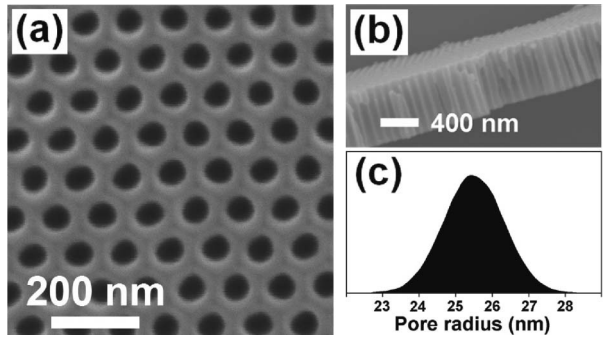

Figure 1. AAO nanopore template: (a) top-surface and (b) cross-sectional view of a thinner (0.8 ± 0.1 μm-thick) membrane observed using scanning electron microscopy. (c) Nanopore structure pore-radius distribution estimated from SEM image analysis.

confinement effects since the critical thickness parameter for deuterated-5CB molecules confined in such membranes would be $R/\xi_0 \approx 154$ (*3*, *61*). As seen in Table 1(a) and (b), such a large critical thickness parameter predicts that the system will follow bulk-like phase transition behaviour with weak paranematic ordering regardless of the substrate potential.

In the present case, the AAO alumina membranes, such as those shown in Figure 1, were fabricated using a previously-described multi-step aluminium anodisation process (*62*, *63*). The resultant nanopore arrays, grown to an 80 ± 5 μm thickness, feature both a 103 ± 5 nm lattice-constant and a narrow 25.5 ± 1.5 nm pore-radius distribution. Due to its small pore diameter, a high degree of uniformity and a much higher surface-to-volume ratio than similar, larger diameter Anopore membranes, this template offers a unique platform to investigate confined liquid crystals using ^{2}H-NMR. Under such conditions (critical thickness parameter $R/\xi_0 \approx 38$ for 5CB), surface interactions are expected to become significant and interesting surface-induced phase-transition behaviours are anticipated when the substrate potential is sufficiently high ($g > 0.012$) (*2*, *3*, *6*, *13–19*).

3.1 Molecular organisation in the nematic phase

In the nematic phase ($T < T_{NI}$), ^{2}H-NMR spectroscopy provides a direct assessment of the molecular organisation inside the cylindrical cavities by monitoring the spectral evolution for the liquid crystal-filled nanopores when the sample is rotated with respect to the **B**-field. From the results shown in Figure 2, one can directly confirm the molecular orientation distribution in the nanopores since $\delta\nu \approx \delta\nu_B$ for $\theta = 0°$ and $\delta\nu \approx \delta\nu_B/2$ for $\theta = 90°$ (*64*), indicating a preferred molecular orientation parallel to the cylindrical pores axis (*6*, *19*, *49*, *50*). By convention, the order parameter

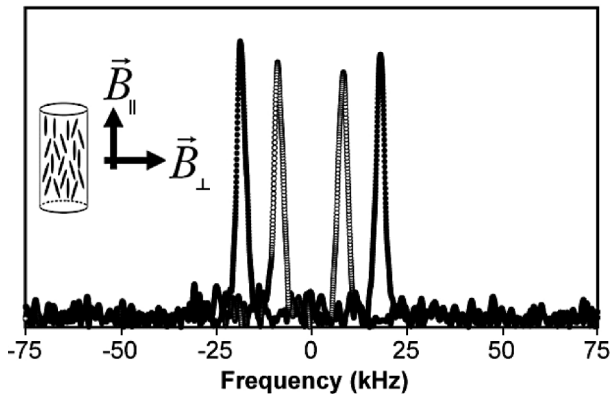

Figure 2. ^{2}H-NMR spectra in the nematic phase with the nanopore axis oriented respectively parallel (●) and perpendicular (○) with respect to the **B**-field at $T - T_{NI} = -5$ K.

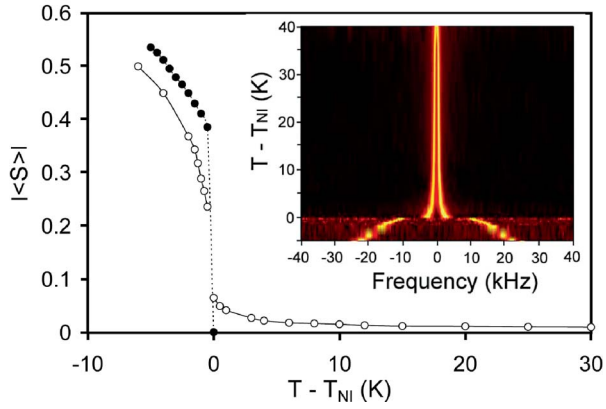

Figure 3. Volume-averaged order parameter $|<S>|$ temperature evolution obtained directly from the ^{2}H-NMR quadrupolar frequency splitting for nano-confined (○) and bulk (●) αd_2-5CB. The inset shows the full ^{2}H-NMR spectrum temperature evolution for the nano-confined molecules.

is generally defined as negative when the molecules are aligned parallel to the pores axis and positive when they are forced to be aligned perpendicular to the pores axis by using a surfactant.

3.2 *Volume-averaged order parameter*

When the temperature is raised over T_{NI}, the surface-induced order parameter inside the cavity can be described as a decaying exponential $|S(r)|=|S_0| \exp[-(R - r)/\xi]$, where r and R are respectively the radial position and the radius of the cylindrical cavity (such that the difference $R - r$ represents the distance to the wall), S_0 is the orientational order parameter at the interface and the exponential decay constant ξ is the correlation or coherence length (*18*, *45*, *48*, *49*, *52*, *60*). This temperature-dependent correlation length is generally described by the LdG theory for second-order phase transitions as $\xi = \xi_0 (T/T^* - 1)^{-\alpha}$ (*18*, *48*, *49*). For the bulk 5CB liquid crystal, $\xi_0 = 0.65$ nm, $\alpha = 0.5$ and the second-order transition temperature $T^* = T_{NI} - 1.1$ K (*6*, *18*, *48–51*).

The residual (paranematic) ordering seen in the inset of Figure 3 originates from a thin surface-anchored molecular layer with a uniform surface order parameter S_0 inducing bulk alignment through short-range elastic interactions explained by the short correlation length above the transition point (*2*, *3*, *6*, *18*, *58–60*). The finite thickness l_0 of this strongly-anchored molecular layer is expected to be between 1.0 and 2.0 nm, depending on the surface energy (*5*, *6*).

The presence of such surface-induced ordering can lead to a residual NMR quadrupolar frequency splitting, even at temperatures well above T_{NI}. As shown in Table 1, this effect is expected to be small in weakly-confined systems where elastic forces from the bulk dominate (*48*). From the previous expression, the correlation length ξ for 5CB corresponds to ≈11 nm at T_{NI}, and diminishes to less than 3.5 nm at temperatures more than 10 K above T_{NI}, which suggests that this surface-induced ordering would occur only very close to the interface due to short-range elastic interactions (*5*, *6*).

Figure 3 compares the volume-averaged order parameter measured from the ^{2}H-NMR spectrum for the nano-confined and bulk liquid crystal systems. The large residual NMR frequency splitting persists at temperatures well above T_{NI}. When the magnetic field is parallel to the pores axis, this residual frequency splitting can be related to the volume-averaged $|<S>|$ and surface-order parameter $|S_0|$ by the following relation (*48*, *56*):

$$\langle \delta\nu \rangle = \frac{\delta\nu_B}{S_B} |\langle S \rangle| \approx \frac{\delta\nu_B}{S_B} \cdot \frac{2|S_0|(\xi + l_0)}{R}, \qquad (3)$$

where the brackets indicate a complete spatial averaging effect. Such an averaging effect can be explained in terms of the characteristic length of diffusion $d \approx (D/\delta\nu)^{1/2}$, where $D \approx 10^{-11}$ m^{-2} sec for 5CB, being comparable to the cavity radius R at temperatures above T_{NI} ($d > 25$ nm for $T - T_{NI} > 3$ K) (*48*). The right side of Equation (3) relies on the approximation that $R >> \xi$, is as shown previously for $T - T_{NI} \geq 0.5$ K (*45*).

3.3 *Paranematic ordering in alumina-based nanopore geometry*

The paranematic frequency-splitting and the associated surface order parameter S_0 temperature-evolution are

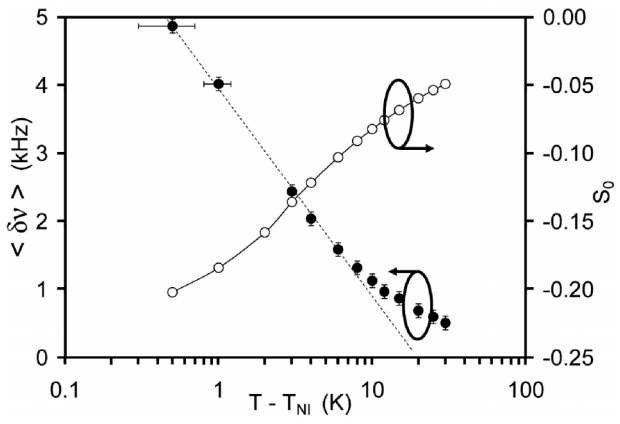

Figure 4. Paranematic ^{2}H-NMR quadrupolar frequency splitting $<\delta\nu>$ and the associated surface order parameter S_0 as a function of temperature. The dotted line highlights the weak logarithmic divergence when approaching T_{NI}, suggesting complete orientational wetting.

highlighted in Figure 4 (remember S_0 is negative by convention, since the preferred molecular orientation is parallel to the pores axis). In this system, large quadrupole frequency splittings were measured, suggesting degrees of ordering far larger than those reported in previous studies of micro-confined systems (*6*, *18*).

Moreover, the weak logarithmic divergence in Figure 4 suggests a complete molecular wetting regime (*6*, *18*). To the authors' knowledge, complete orientational wetting has not been previously observed in confined systems (*6*, *13*, *19*, *20*). Surface wetting is known to relate to the surface adsorption parameter (*65*). Since the surface adsorption is directly proportional to the NMR splitting and, therefore, is inversely proportional to the cavity size R, surface adsorption and wetting should indeed be strongly favoured in such nano-confined systems. Strong molecular wetting can be expected since these as-grown AAO membranes are known to be hydrophobic.

From the experimental data shown in Figure 4, one can directly obtain the temperature-independent S_{00} surface-order coefficient from the LdG theory and the corresponding surface-anchored molecular-layer effective thickness l_0 by fitting the temperature dependence of $<\delta\nu>$ using the following equation (*56*):

$$\langle\delta\nu\rangle = \frac{\delta\nu_B}{S_B}\cdot\frac{|S_{00}|}{R}\left(\frac{\xi_0}{\frac{T}{T^*}-1}+\frac{l_0}{\sqrt{\frac{T}{T^*}-1}}\right), \qquad (4)$$

using the second order transition temperature $T^* \equiv T_{NI} - \beta$, $R = 25$ nm, $\delta\nu_B/S_B \approx 87.5$ kHz and $\xi_0 = 0.65$ nm for 5CB. The optimal fitting yields $S_{00} = 0.0135 \pm 0.001$, $\beta = 1.5 \pm 0.1$ K and $l_0 = 1.73 \pm 0.15$ nm, which is in good agreement with previous reports (*6*, *17–19*, *48*, *49*).

Interestingly, the second-order transition temperature T^* appears to be slightly lower due to the strong confinement, as suggested by the increased β obtained from the fit, which is also in good agreement with theoretical expectations (*3*, *19*, *61*) and numerical simulations (*66*). Therefore, the surface-order parameter S_0 can be directly obtained at any given paranematic temperature using the expression (*56*)

$$S_0 = \frac{1}{2}\frac{S_{00}}{\sqrt{\frac{T}{T^*}-1}}, \qquad (5)$$

with the known entities $S_{00} = 0.0135 \pm 0.001$ and $T^* = T_{NI} - 1.5$ K. The temperature-independent surface-order coefficient S_{00} is directly equivalent to the substrate potential g, sometimes used in the LdG theory (*3*).

3.4 Nematic surface order parameter

Another interesting observation stems from the quadrupole frequency splitting comparison of the confined and bulk systems displayed in Figure 3. In the nematic phase, the confined system shows a quadrupole frequency splitting (and order parameter) that is noticeably weaker than the bulk. With $T > T_{NI}$, we have shown that surface interactions induce a significant degree of ordering in the isotropic phase by surface-anchoring. From similar reasoning, surface interactions can introduce a finite degree of disordering in the bulk nematic distribution ($T < T_{NI}$) (*12, 67–69*). This surface-induced disordering also decays exponentially when moving away from the pore surface, giving rise to an averaged order parameter observed in the ^{2}H-NMR that is smaller than the bulk order parameter S_B. Far from the surface, volume effects dominate and the order parameter is equal to the bulk (*68*). Even in the nematic phase, one also measures a spatially-averaged ^{2}H-NMR frequency splitting due to the strong nanoscale confinement. Such an assumption is justified, considering the diffusion length $d \approx (D/\delta\nu)^{1/2}$ still being comparable to the cavity radius R even in the nematic phase ($d \approx 22$ nm for $T - T_{NI} = -0.5$ K and $d \approx 15$ nm for $T - T_{NI} = -5$ K). Considering the nanometre scale cavity radius R, we can safely assume that the correlation length in the nematic phase is much longer than the nanometre-scale pore radius ($\xi >> R$), such that surface effects dominate and the volume-averaged order parameter $<S>$ obtained directly from the ^{2}H-NMR quadrupolar frequency splitting measured in the nematic phase ($T < T_{NI}$) is equal to the surface-order parameter S_0 (*45*).

3.5 Surface order parameter and substrate potential

Temperature evolution for the confined surface-order parameter S_0 can be obtained directly from the ^{2}H-NMR spectra temperature evolution, both in the nematic and the paranematic phases, using the left side of Equation (3) and Equation (5), respectively. As shown in Figure 5, a continuous surface-order parameter S_0 evolution from the nematic phase ($T - T_{NI} = -5$ K) up to deep into the paranematic phase ($T - T_{NI} = 30$ K) was measured for the nano-confined system. The bulk αd_2-5CB liquid crystal order parameter S_B temperature-evolution is also displayed for comparison.

As shown in Table 1, the continuous evolution of S_0 through the bulk nematic–isotropic phase transition shown in Figure 5 requires both a strong surface energy G/A and nano-confinement (*2*, *3*, *69*) to overcome the volume energy. The surface energy can be obtained directly from the LdG theory using the temperature-independent surface-order parameter since $G/A = S_{00}\,(a\,L\,T^*)^{1/2} = (3.54 \pm 0.25)\cdot 10^{-4}$ J m^{-2} where a, L and T^* are material-dependent parameters known for 5CB and where the dimensionless substrate potential $g = S_{00} = 0.0135$ (*2*, *3*, *19*, *56*).

3.6 Discussion on confinement in the alumina-based nanopore geometry

In the present case, we have shown experimentally that the substrate potential $g \approx 0.0135$ and the critical film thickness parameter $R/\xi_0 \approx 38$ correspond to the case shown in Table 1(d). As expected, the order parameter temperature-evolutions in our nano-confined system show a unique molecular state with no complete second-order phase-transition at the interface (S_0), combined with an abrupt discontinuity in the averaged-order parameter $<S>$, suggestive of a dominant second-order phase-transition in the centre of the nanopores, which is consistent with theoretical predictions (*2*, *3*). To the best of our knowledge, this unique phase-transition behaviour theoretically predicted more than three decades ago has never been experimentally observed before, most likely due to the difficulties in obtaining a porous nanopore template offering both the small pore diameter and the high pore-diameter uniformity enabled by the AAO nanopore array.

Moreover, the measured $|S_0| \approx 0.2$ at T_{NI} for $g > 0.012$ and $R/\xi_0 \approx 38$ is also consistent with theoretical predictions for such confined system (*2*, *3*). The critical transition temperature was slightly increased due to confinement, as suggested by the increased β obtained by fitting the experimental results ($\beta \approx 1.5$ K for the confined system and $\beta \approx 1.1$ K for the bulk) (*19*, *56*), which is also in good agreement with theoretical expectations (*2*, *3*, *61*) and numerical simulations (*66*).

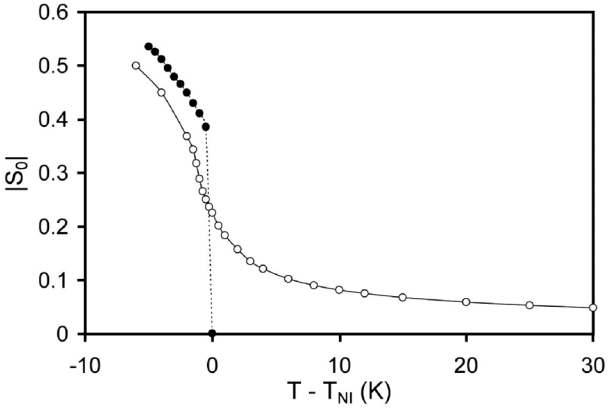

Figure 5. Absolute surface-order parameter $|S_0|$ from the nano-confined system. The bulk order parameter S_B (●) is displayed as a comparison.

4. Surface-induced ordering in nanoscale-sized PDLC droplets

The PDLC films used in this study consist of dispersions of ad_2-5CB and polyvinyl alcohol PVA205 [molecular weight: 25,000, degree of hydrolysis: 88%, Kuraray Co., Ltd.], which is a water soluble polymer. A 20 wt % aqueous solution of polyvinyl alcohol (PVA) was mixed with the liquid crystal and then dispersed in water. An ultrasonic processor (400 W, 20 kHz, Cole-Parmer Instrument Co.) at 40% output with a 1/8 in. microtip was used to emulsify the liquid crystal into the PVA aqueous solution. The emulsion is coated onto a smooth polyethylene terephthalate (PET) substrate using a Meyer Bar. All processing is done under ambient conditions. After the water evaporated, the polymer film was carefully released from the substrate by peeling it away from the end. The film thickness was approximately 16 ± 4 μm and the concentration of liquid crystal in the film was 25 wt %. The film was stretched to the desired strain of 5%, 20%, 100%, and 400%, cut into strips 20 mm by 6 mm, stacked such that the thickness was more than 50 μm, and carefully inserted into a NMR tube. Figure 1(a) shows scanning electron microscope (SEM) images of a PDLC film before stretching, when the droplets are approximately spherical.

After stretching, the droplets become elongated, with their major axes along the stretch direction. The stretching is accompanied by an alignment of the nematic director parallel to the stretch direction within each droplet. This is confirmed using optical polarisation measurements (*39*, *40*). The average diameter of the unstretched droplets was measured to be 92 ± 16 nm. Assuming that the liquid crystal droplet was

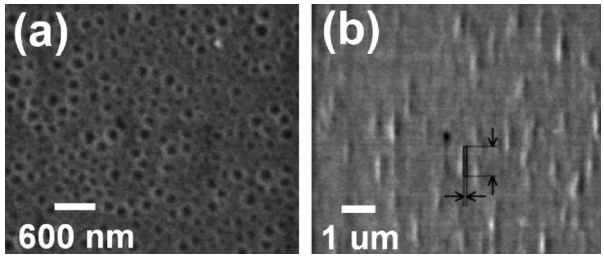

Figure 6. SEM micrographs of the unstretched and 100%-strained PDLC droplets. (a) PDLC films before stretching. The diameter of the droplets is 92 ± 16 nm. (b) Conformation of the droplets after stretching with 400% strains. The arrows indicate that the major and minor axis lengths of the ellipsoid-shaped droplets are estimated at 460 ± 80 nm and 41 ± 7 nm, respectively (averaged over more than 100 droplets).

incompressible and its initial shape was spherical, the minor and major semiaxis lengths after stretching can be approximated as $R_0 \approx R_{\text{ini}}(1+\varepsilon)^{-1/2}$ and $Z_0 \approx R_{\text{ini}}(1+\varepsilon)$ respectively, where R_{ini} is the initial radius and ε is the tensile strain. Using those expressions, the aspect ratio of the strained droplets can be defined as:

$$\rho \equiv \frac{Z_0}{R_0} \approx (1+\varepsilon)^{3/2}. \quad (6)$$

Note that even at zero strain the droplet shapes of these systems are not perfectly spherical, but are close to oblate spheroids with their minor axes perpendicular to the film plane (*40*). Then, assuming the Poisson ratio to be isotropic (*39*, *40*), Equation (6) is still valid when we define R_{ini} as the initial length of one of the principal axes. Figure 6(b) shows the droplets after they have been subjected to 400% strain. The stretched PDLC film was stacked in the NMR tube such that the stretched axis of the film, and therefore the long axis of the droplets, was nicely aligned parallel to the magnetic field direction.

4.1 Molecular organisation in the nematic phase

In this case, ^{2}H-NMR was used to study the molecular organisation inside the unstretched and stretched droplets. Figure 7(a) depicts the droplet organisation in the unstretched PDLC films. The ^{2}H-NMR analysis displayed in Figure 7(b), measured at $T - T_{NI} = -4$ K with the magnetic field oriented in the plane and perpendicular to the PDLC film, confirms that the molecules align predominantly in the plane of the PDLC layer (*40*). As shown in Figure 7(b), the Pake-type powder spectrum suggests both a two-dimensional random distribution of the molecules in the plane of the film and a dominant bipolar molecular ordering inside the droplets, as depicted in Figure 7(a) (*29*, *30*, *40*, *55*).

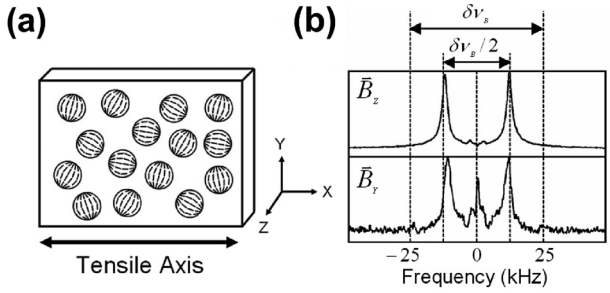

Figure 7. Nematic molecular orientation in the unstretched PDLC droplets. (a) Schematics of the PDLC droplet organisation before stretching. (b) ^{2}H-NMR spectrum measured at $T - T_{NI} = -4$ K with the field oriented perpendicular ($\mathbf{B}_Z$) and parallel to the plane of the film ($\mathbf{B}_Y$).

On the other hand, Figure 8(a) depicts the droplet organisation in the stretched PDLC films. Under 100% tensile strains, the ^{2}H-NMR analysis displayed in Figure 8(b), and performed with the magnetic field oriented out-of plane and parallel to the plane (both perpendicular and parallel to the strain axis), confirms that the stretched droplets align predominantly in the plane of the film and along the strain axis.

When the field is oriented perpendicular to the strain axis, the splitting approaches half the splitting of the bulk. However, the splitting measured with the field oriented along the tensile axis increases with the level of strain to approach the bulk splitting under high strains, suggesting a strong molecular ordering along this axis (*40*). The large splitting measured this way (similar to the cylindrical geometry) provides a significant advantage when studying the phase-transition behaviour in such a nano-confined system.

4.2 Paranematic ordering in the strained PDLC droplet geometry

We then measured the ^{2}H-NMR quadrupolar splitting for the 5%, 20%, 100% and 400% strained PDLC films through the nematic-paranematic transition. As shown in Figure 9, the residual ordering measured above the transition dramatically increases as the droplets are stretched and persisted far above the bulk transition temperature for 5CB. In this geometry, the expression for the ^{2}H-NMR frequency splitting can be related to the surface-order parameter S_0 through the following relation (*40*):

$$\langle \delta\nu \rangle = \frac{\delta\nu_B}{S_B} |\langle S \rangle| \approx \frac{\delta\nu_B}{S_B} \cdot \frac{3|S_0|(l_0+\xi)}{4R_{ini}(1+\varepsilon)^{-1/2}} E(\rho), \quad (7)$$

where l_0 represents the same previously-defined surface-anchored molecular-layer effective thickness and the coefficient $E(\rho)$ is defined as:

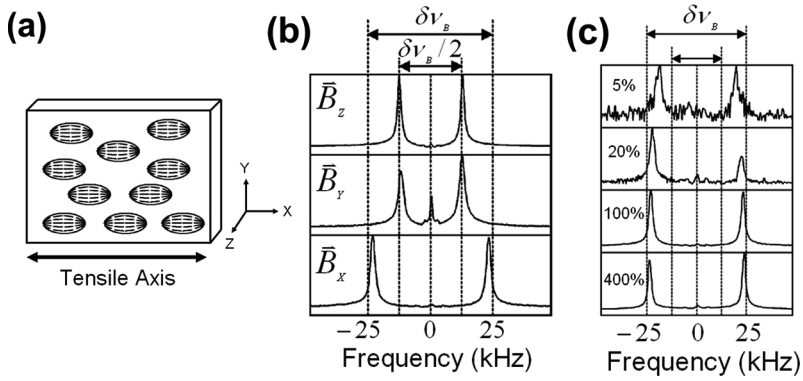

Figure 8. Nematic molecular orientation in the strained PDLC droplets. (a) Schematics of the PDLC droplet organisation under tensile strains. (b) ^{2}H-NMR spectrum measured at $T - T_{NI} = -4$ K with the field oriented perpendicular to the plane ($\mathbf{B}_Z$), parallel to the plane but perpendicular to the tensile axis ($\mathbf{B}_Y$) and parallel to the 100% tensile strain axis ($\mathbf{B}_X$). (c) ^{2}H-NMR spectrum measured at $T - T_{NI} = -4$ K with the field oriented parallel to the tensile strain axis ($\mathbf{B}_X$) for the PDLC films subjected to 5%, 20%, 100% and 400% tensile strain.

$$E(\rho) = \frac{2\rho^2 + 1}{\rho(\rho^2 - 1)} + \frac{\rho(2\rho^2 - 5)}{(\rho^2 - 1)^{3/2}} \arctan\left(\sqrt{\rho^2 - 1}\right), \qquad (8)$$

where ρ is the aspect ratio of the stretched ellipsoid as defined by Equation (6). Using the temperature-dependent expressions for ξ and S_0, derived from the LdG theory, one can directly obtain the following expression for the frequency splitting measured from the ellipsoid geometry of the stretched PDLC droplets (equivalent to Equation (4) in the cylindrical geometry):

$$\langle \delta\nu \rangle = \frac{\delta\nu_B}{S_B} \cdot \frac{3S_{00}E(\rho)}{8R_{ini}(1+\varepsilon)^{-1/2}} \left(\frac{\xi_0}{\frac{T}{T^*} - 1} + \frac{l_0}{\sqrt{\frac{T}{T^*} - 1}} \right), \qquad (9)$$

where $\delta\nu_B/S_B \approx 87.5$ kHz, $\xi_0 = 0.65$ nm and $T^* \equiv T_{NI} - \beta$ K for 5CB and $R_{\text{ini}} \approx 46 \pm 8$ nm. Using this

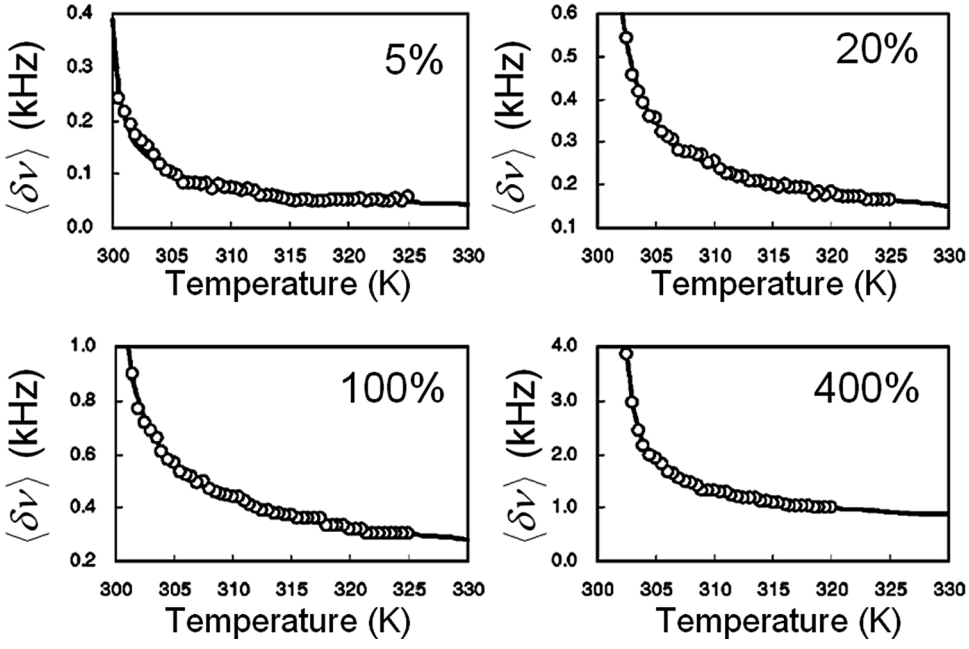

Figure 9. Paranematic ordering in the strained PDLC droplets. ^{2}H-NMR quadrupolar frequency splitting temperature evolution measured above the nematic–paranematic transition for the PDLC films subjected to 5%, 20%, 100% and 400% tensile strains. The paranematic ordering drastically increases as the PDLC films are strained. The plain lines show the optimum data fit obtained using Equation (9).

Table 2. Overview of the optimum data-fitting parameters obtained from the 5%, 20%, 100% and 400% strained PDLC films. The values for the longitudinal and transverse critical thickness parameters (R_0/ξ_0 and Z_0/ξ_0) are approximated using $R_0 \approx R_{ini}(1+\varepsilon)^{-1/2}$ and $Z_0 \approx R_{ini}(1+\varepsilon)$, respectively.

Strains	l_0 (nm)	β (K)	g	R_0/ξ_0	Z_0/ξ_0
5%	0.7	0.64	0.023	69	74
20%	1.5	1.29	0.033	64	85
100%	1.8	1.30	0.033	50	142
400%	2.4	0.33	0.017	31	354

expression for a given tensile strain (known ε and ρ), it is now possible to directly obtain the second-order transition temperature shift β, the surface-anchored molecular-layer effective thickness l_0 and the temperature-independent S_{00} surface-order coefficient by fitting the ^{2}H-NMR frequency splitting evolution as a function of temperature, as shown in Figure 9.

The values obtained for the surface-anchored molecular layer thickness l_0, the second-order transition-temperature shift β, and the temperature-independent substrate potential g as a function of the applied strains are summarised in Table 2. These results are consistent with the Monte Carlo analysis predictions for the stretched PDLC system (*40*).

4.3 Discussion on confinement in the PDLC-based droplet geometry

For the stretched PDLC geometry, it is a little trickier to interpret the results shown in Table 2 in light of the phase-transition behaviours predicted in Table 1. In contrast with the nanopore system, a residual paranematic ordering combined with discontinuous phase-transition behaviour was observed both in the bulk and at the interface. For the unstretched or weakly-strained droplets, while the substrate potential seems large enough to generate continuous phase transition behaviour, the critical thickness parameter appears too large to do so. Therefore, we observe behaviour similar to the case (b) described in Table 1. A small β measured for the weakly-strained samples is consistent with this hypothesis. When subjected to 20% and 100% strains, the substrate potential seems to increase while the critical thickness parameter along the minor axis decreases. Yet, the continuous phase-transition behaviour was not observed. However, Sheng's model summarised in Table 1 is for a semi-infinite system with a free surface. In the cylinder topology, the system can be visualised as a curved surface with the free surface in the centre of the pore and both ends are open (free). In the 20% and 100% stained droplets, the surface-induced ordering along the minor and major axis are more likely to compete together. While the critical thickness parameter goes down along the minor axis, it clearly increases along the major axis, as shown in Table 2. On its own, this is probably enough to prevent seeing the continuous phase transition behaviour at the surface seen with the nanopore system. Then, for larger strains, the substrate potential seems to drop significantly even though the critical thickness parameter along the minor axis also decreases. This is also consistent with the smaller β measured for the 400% sample.

5. Conclusions

In summary, molecular self-organisation in two nano-confined systems was studied using ^{2}H-NMR spectroscopy of αd_2-5CB liquid crystals. In a highly-uniform AAO nanopore platform, we found that the confined molecular organisation in the nematic phase follows a parallel axial distribution (*45*). A model was presented to extract the surface-order parameter in both the nematic and the paranematic phases from the ^{2}H-NMR spectrum temperature evolution. The quadrupole frequency splitting observed up to 40 K above the bulk nematic–isotropic transition temperature (T_{NI}) demonstrates the existence of a 1.7 nm-thick surface-pinned molecular layer at the solid–liquid crystal interface. The orientational surface-order coefficient (S_{00}) indicates a high degree of paranematic ordering in comparison with previous reports using bulk and micro-confined systems (*6*, *18*, *48*, *49*). The high surface energy (3.54×10^{-4} J m^{-2}) and nano-confinement that lead to such strong surface-induced ordering deep in the bulk isotropic phase also lead to a finite degree of surface-induced disorder in the nematic phase (*45*). A unique surface-induced molecular phase with a complete orientational wetting regime, as well as a continuous surface-order (S_0) and discontinuous averaged order-parameter $<S>$ evolution through the nematic–paranematic transition, was observed (*45*) as theoretically predicted for molecular films with a thickness ($\approx R$) between 16 and 65 nm combined with a high surface-energy (*2*, *3*).

For the strained PDLC nano-droplet system, the ^{2}H-NMR analysis in the nematic phase revealed that the molecular alignment in the droplets lies predominantly in the plane of the film. Under tensile strains, the spherical droplets become ellipsoid-shaped with their major axis oriented along the tensile strain axis, forcing the molecules to align in the same direction. The paranematic ordering was also studied by NMR and analysed using the LdG theory, and an elliptical model was developed to describe the paranematic surface-induced ordering. Through this model, the surface-induced order parameter was found to increase and become

less temperature-dependent under moderate strains, which is consistent with previous optomechanical measurements (*39*) and Monte Carlo model analysis (*40*). Moreover, the PDLC matrix chains appear to disentangle and modify surface anchoring conditions under high strains, which is also consistent with previous models and observations (*39*, *40*). This PDLC geometry is appealing since it offers a platform where the balance between surface and volume energies can by externally tuned through tensile strains, a potentially useful feature to allow deeper studies of surface-induced ordering behaviours.

This capability to control and preserve molecular ordering using nano-confined systems could be useful in a variety of self-organisation applications, and helpful in providing insights into the collective behaviours of strongly cooperative molecular systems.

References

(1) de Gennes, P.G. *Mol. Cryst. Liq. Cryst.* **1971**, *12*, 193–214.
(2) Sheng, P. *Phys. Rev. Lett.* **1976**, *37*, 1059–1062.
(3) Sheng, P. *Phys. Rev. A* **1982**, *26*, 1610–1617.
(4) Sluckin, T.J.; Poniewierski, A. *Fluid Interfacial Phenomena*, Croxton, C.A., Ed.; Wiley: New York, 1986; ch 5.
(5) Crawford, G.P.; Ondris-Crawford, R.J.; Doane, J.W.; Žumer, S. *Phys. Rev. E* **1996**, *53*, 3647–3661.
(6) Crawford, G.P.; Ondris-Crawford, R.; Žumer, S.; Doane, J.W. *Phys. Rev. Lett.* **1993**, *70*, 1838–1841.
(7) Miyano, K. *Phys. Rev. Lett.* **1979**, *43*, 51–54.
(8) Miyano, K. *J. Chem. Phys.* **1979**, *71*, 4108–4111.
(9) Guyot-Sionnest, P.; Hsiung, H.; Shen, Y.R. *Phys. Rev. Lett.* **1986**, *57*, 2963–2966.
(10) Barberi, R.; Durand, G. *Phys. Rev. A* **1990**, *41*, 2207–2210.
(11) Chen, W.; Martinez-Miranda, L.J.; Hsiung, H.; Shen, Y.R. *Phys. Rev. Lett.* **1989**, *62*, 1860–1863.
(12) Moses, T.; Shen, Y.R. *Phys. Rev. Lett.* **1991**, *67*, 2033–2036.
(13) Crawford, G.P.; Yang, D.K.; Žumer, S.; Finotello, D.; Doane, J.W. *Phys. Rev. Lett.* **1991**, *66*, 723–726.
(14) Crawford, G.P.; Stannarius, R.; Doane, J.W. *Phys. Rev. A* **1991**, *44*, 2558–2569.
(15) Crawford, G.P.; Allender, D.W.; Doane, J.W. *Phys. Rev. A* **1992**, *45*, 8693–8708.
(16) Allender, D.W.; Crawford, G.P.; Doane, J.W. *Phys. Rev. Lett.* **1991**, *67*, 1442–1445.
(17) Ondris-Crawford, R.J.; Crawford, G.P.; Žumer, S.; Doane, J.W. *Phys. Rev. Lett.* **1993**, *70*, 194–197.
(18) Crawford, G.P.; Žumer, S. *Liquid Crystals in Complex Geometries*, Crawford, G.P. and Zumer, S., Eds.; Taylor & Francis: Bristol, 1996; pp 1–19.
(19) Crawford, G.P.; Allender, D.W.; Doane, J.W.; Vilfan, M.; Vilfan, I. *Phys. Rev. A* **1991**, *44*, 2570–2577.
(20) Ziherl, P.; Vilfan, M.; Vrbanèiè-Kopaè, N.; Žumer, S.; Ondris-Crawford, R.J.; Crawford, G.P. *Phys. Rev. E* **2000**, *61*, 2792–2798.
(21) Jin, T.; Crawford, G.P.; Ondris-Crawford, R.J.; Žumer, S.; Finotello, D. *Phys. Rev. Lett.* **2003**, *90*, 015504-1–015504-4.
(22) Iannacchione, G.S.; Crawford, G.P.; Žumer, S.; Doane, J.W.; Finotello, D. *Phys. Rev. Lett.* **1993**, *71*, 2595–2598.
(23) Iannacchione, G.S.; Crawford, G.P.; Qian, S.; Doane, J.W.; Finotello, D.; Žumer, S. *Phys. Rev. E* **1996**, *53*, 2402–2411.
(24) Iannacchione, G.S.; Qian, S.H.; Crawford, G.P.; Keast, S.S.; Neubert, M.E.; Doane, J.W.; Finotello, D.; Steele, L.M.; Sokol, P.E.; Žumer, S. *Mol. Cryst. Liq. Cryst. Sci. Technol. Sect. A* **1995**, *262*, 13–23.
(25) Kralj, S.; Lahajnar, G.; Zidanšek, A.; Vrbanèiè-Kopaè, N.; Vilfan, M.; Blinc, R.; Kosec, M. *Phys. Rev. E* **1993**, *48*, 340–349.
(26) Finotello, D.; Zeng, H.; Zalar, B.; Iannacchione, G.S. *Mol. Cryst. Liq. Cryst. Sci. Technol. Sect. A* **2001**, *358*, 237–250.
(27) Zalar, B.; Blinc, R.; Žumer, S.; Jin, T.; Finotello, D. *Phys. Rev. E* **2002**, *65*, 041703-1–041703-16.
(28) Ziherl, P.; Zumer, S. *Phys. Rev. Lett.* **1997**, *78*, 682–685.
(29) Golemme, A.; Žumer, S.; Doane, J.W.; Neubert, M.E. *Phys. Rev. A* **1988**, *37*, 559–569.
(30) Golemme, A.; Žumer, S.; Allender, D.W.; Doane, J.W. *Phys. Rev. Lett.* **1988**, *61*, 2937–2940.
(31) Sheng, P.; Shen, Y. R. *Bull. Am. Phys. Soc.* **1981**, *26*, 275–275.
(32) Vilfan, I.; Vilfan, M.; Žumer, S. *Phys. Rev. A* **1989**, *40*, 4734–4730.
(33) Fuh, A.; Lin, T.H. *J. Appl. Phys*. **2004**, *96*, 5402–5404.
(34) Liu, Y.J.; Sun, X.W.; Dai, H.T.; Liu, J.H.; Xu, K.S. *Opt. Mater.* **2005**, *27*, 1451–1455.
(35) Pasini, P.; Zannoni, C., Eds.; *Advances in the Computer Simulations of Liquid Crystals*, Kluwer: Dordrecht, 2000.
(36) Chiccoli, C.; Pasini, P.; Skaèej, G.; Zannoni, C.; Žumer, S. *Phys. Rev. E* **1999**, *60*, 4219–4225.
(37) Chiccoli, C.; Pasini, P.; Skaèej, G.; Zannoni, C.; Žumer, S. *Phys. Rev. E* **2000**, *62*, 3766–3774.
(38) Bharadwaj, R.K.; Bunning, T.J.; Farmer, B.L. *Liq. Cryst.* **2000**, *27*, 591–603.
(39) Amimori, I.; Priezjev, N.V.; Pelcovits, R.A.; Crawford, G.P. *J. Appl. Phys.* **2003**, *93*, 3248–3252.
(40) Amimori, I.; Eakin, J.N.; Qi, J.; Skacej, G.; Žumer, S.; Crawford, G.P. *Phys. Rev. E* **2005**, *71*, 031702-1–031702-11.
(41) Bates, M.A. *Soft Matter* **2008**, *4*, 2059–2063.
(42) Zhang, Z.; van Duijneveldt, J.S. *Soft Matter* **2007**, *3*, 596–604.
(43) Yoshino, K.; Ozaki, R.; Matsumoto, J.; Ojima, M.; Hiwatashi, S.; Matsuhisa, Y.; Ozaki, M. *IEEE Trans. Dielectr. Electr. Insul.* **2006**, *13*, 678–686.
(44) Jian, K.Q.; Hurt, R.H.; Sheldon, B.W.; Crawford, G.P. *Appl. Phys. Lett.* **2006**, *88*, 163110-1–163110-3.
(45) Cloutier, S.G.; Eakin, J.N.; Guico, R.S.; Sousa, M.E.; Crawford, G.P.; Xu, J.M. *Phys. Rev. E* **2006**, *73*, 051703-1–051703-7.
(46) Drzaic, P.S. *Liquid Crystal Dispersions*; World Scientific: Singapore, 1995.
(47) Aphonin, O.A.; Panina, Yu. V.; Pravdin, A.B.; Yakovlev, D.A. *Liq. Cryst.* **1993**, *15*, 395–407.
(48) Doane, J.W.; Crawford, G.P. *Encyclopaedia of Nuclear Magnetic Resonance*; John Wiley and Sons: New York, 1995.

(49) Doane, J.W.; Vaz, N.A.; Wu, B.G.; Žumer, S. *Appl. Phys. Lett.* **1986**, *48*, 269–271.
(50) Coles, H.J. *Mol. Cryst. Liq. Cryst.* **1978**, *49*, 67–74.
(51) Chandrasekhar, S. *Liquid Crystals*; Cambridge University Press: London, 1977.
(52) deGennes, P.G. *Physics of Liquid Crystals*; Clarendon: Oxford, 1974.
(53) Zalar, B.; Žumer, S.; Finotello, D. *Phys. Rev. Lett.* **2000**, *84*, 4866–4869.
(54) Schopohl, N.; Sluckin, T.J. *Phys. Rev. Lett.* **1987**, *59*, 2582–2584.
(55) Dong, R.Y. *Nuclear Magnetic Resonance of Liquid Crystals*; Springer: New York, 1997; 2nd Edn.
(56) Crawford, G.P.; Vilfan, M.; Doane, J.W.; Vilfan, I. *Phys. Rev. A* **1991**, *43*, 835–842.
(57) Crawford, G.P.; Steele, L.M.; Ondris-Crawford, R.; Iannacchione, G.S.; Yeager, C.J.; Doane, J.W.; Finotello, D. *J. of Chem. Phys.* **1992**, *96*, 7788–7796.
(58) Vilfan, M.; Zalar, B.; Fontecchio, A.K.; Vilfan, M.; Escuti, M.J.; Crawford, G.P.; Žumer, S. *Phys. Rev. E* **2002**, *66*, 021710-1–021710-9.
(59) Vilfan, M.; Vrbanèiè-Kopaè, N.; Zalar, B.; Žumer, S.; Crawford, G.P. *Phys. Rev. E* **1999**, *59*, R4754–R4757.
(60) Vilfan, M.; Zalar, B.; Crawford, G.P.; Finotello, D.; Žumer, S. *Surfaces and Interfaces of Liquid Crystals*, Rasing, T. and Musevic, I., Eds.; Springer: Berlin, 2004; pp 17–40.
(61) Batalioto, F.; Evangelista, L.R.; Barbero, G. *Phys. Lett. A* **2004**, *324*, 198–202.
(62) Cloutier, S.G.; Hsu, C.H.; Kossyrev, P.A.; Xu, J. *Adv. Mater.* **2006**, *18*, 841–844.
(63) Liang, J.; Chik, H.; Yin, A.; Xu, J. *J. Appl. Phys.* **2002**, *91*, 2544–2546.
(64) Marinelli, M.; Mercuri, F.; Zammit, U.; Scudieri, F. *Phys. Rev. E* **1998**, *58*, 5860–5866.
(65) Blinov, L.M.; Chagrinov, V.G. *Electrooptic Effects in Liquid Crystal Materials*; Springer: New York, 1996.
(66) Marroum, R.M.; Iannacchione, G.S.; Finotello, D. Lee, M.A. *Phys. Rev. E* **1995**, *51*, R2743–R2746.
(67) Ziherl, P.; Sarlah, A.; Žumer, S. *Phys. Rev. E* **1998**, *58*, 602–609.
(68) Barbero, G.; Durand, G. *Liquid Crystals in Complex Geometries*, Crawford, G.P. and Žumer, S., Eds3; Taylor & Francis: Bristol, 1996: pp 21–52.
(69) Sarlah, A.; Žumer, S. *Surfaces and Interfaces of Liquid Crystals*, Rasing, T. and Musevic, I., Eds.; Springer: Berlin, 2004; pp 249–279.